TOWARDS THE ADOPTION OF NEURAL-NETWORK-BASED SOLVERS FOR COUPLED MH-PCM HYDROGEN STORAGE DEVICES

Vesselin K. Krastev[1]*, M. Baldelli[2], L. Bartolucci[2], G. Falcucci[1], V. Mulone[2], S. Cordiner[2]

[1]University of Rome "Tor Vergata", Enterprise Engineering Department, 00133 Rome, Italy

[2]University of Rome "Tor Vergata", Industrial Engineering Department, 00133 Rome, Italy

*Corresponding Author: krastev@dii.uniroma2.it

ABSTRACT

In the present work, recent advancements are shown in the development of neural network-based (NN) numerical solvers for the simulation of the coupled chemistry and physics typical of intermetallic Metal Hydride – Phase Change Material (IMH-PCM) hydrogen storage tanks. The final aim of this research activity is to obtain fast and reliable numerical tools, which should be able to span a large number of different IMH-PCM configurations and thus effectively support the optimal design of the tank in terms of energy density and specific power delivery.
The results shown here include: i) a NN training phase, based on a subset of CFD-generated data, and ii) initial tests of the NN-based solver which is applied out of the training set points to estimate the MH-PCM performance in terms of heat fluxes and hydrogen mass flow rate.
Our findings show great potential in NN-based approaches to reduce simulation turnaround times for this class of complex hydrogen storage systems, thus paving the way for their efficient integration in real-time modelled hydrogen energy systems and their adoption as design tools for IMH-PCM devices.

1 INTRODUCTION

Intermetallic Metal Hydrides (IMH) are particularly attractive solid-state hydrogen carriers, due to the inherent safety and efficiency guaranteed by their moderate operating pressure and temperature, as well as their potential to significantly reduce volumetric footprint per stored kg of hydrogen (Drawer et al., 2024; Pasquini et al., 2022). During the last decade IMHs have undergone significant developments, reaching a limited commercial availability and being forecasted to play a significant role in the small and medium scale hydrogen storage market by 2040 (Drawer et al., 2024). A crucial aspect of the efficient IMHs operation as hydrogen carriers is the system thermal management, which should account for the highly exothermic/endothermic reactions that take place during hydrogenation/dehydrogenation of the metal alloy (Nguyen & Shabani, 2021). A popular passive thermal management option is the coupling of IMHs with Phase Change Materials (PCMs) that act as thermal sink (during hydrogenation) or source (during dehydrogenation) thanks to their latent heat storage capacity (Facci et al., 2021; Kukkapalli et al., 2023; Nguyen et al., 2022; Sreeraj et al., 2022).
The effective design of IMH-PCM storage tanks, as well as their efficient integration with stationary or mobile hydrogen energy systems, requires high-fidelity multiphysics modelling such as Computational Fluid Dynamics (CFD) – based methodologies (Alqahtani et al., 2020; Bartolucci & Krastev, 2022; Chibani et al., 2022; El Mghari et al., 2019). Standard CFD methods are time consuming and do not usually allow for testing many IMH-PCM system configurations and/or operating conditions. A viable alternative is represented by data-driven approaches, which can produce fast yet sufficiently reliable modelling for a variety of engineering systems. An increasing number of Neural-Network-based (NN) solver applications can be found in the literature, dealing separately with PCM-based thermal storage units (He et al., 2024; Maalla et al., 2024; Ouro-Koura et al., 2024) or different aspects of IMH-based hydrogen storage optimisation (Şenol et al., 2024). However, to the best of the authors' knowledge, no IMH-PCM study through NN is currently reported, thus leaving a research gap in that field.

https://doi.org/10.52202/077185-0067

In the present paper, we show our more recent progress in the development of NN solvers for IMH-PCM systems' simulation. As a basic assumption, we use an already established CFD workflow to generate training data for the NN solver. The remainder of the paper is organised as follows: in Section 2, the reference CFD model is introduced, followed by the definition of the NN; in Section 3, results from the NN training and test phases are shown and briefly discussed; in Section 4, conclusions and perspectives for future work are drawn.

2 MATERIALS & METHODS

2.1 CFD model

The IMH-PCM tank geometry and computational domain are displayed in Fig. 1. This is equivalent to the jacket-type system that has been already optimised for constant (atmospheric) pressure discharge operation in a previous publication from the authors (V. Krastev et al., 2023). The IMH is a La-based AB_5 alloy, while for the PCM two options are considered at first: an inorganic salt hydrate (*PCM1*) and an organic paraffin-type material (*PCM2*), both initially selected to match the IMH equilibrium temperature in atmospheric pressure discharge conditions (V. Krastev et al., 2023). The most relevant IMH and PCM properties are listed in Tables 1 and 2.

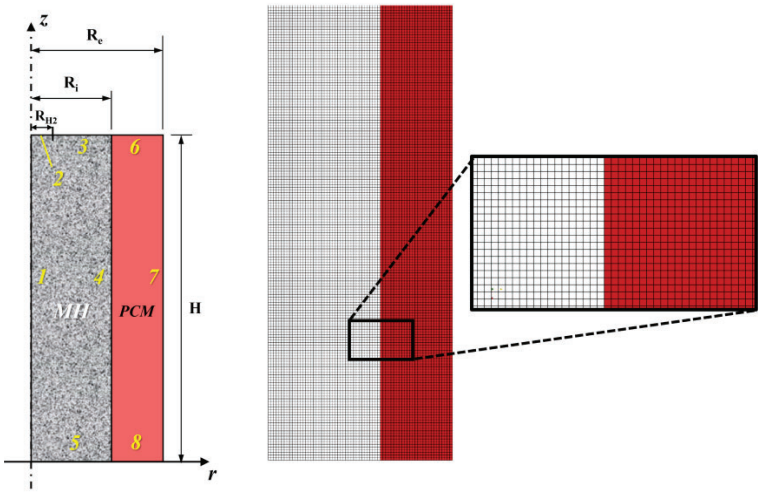

Figure 1: Schematics of the IMH-PCM jacket configuration and computational mesh. Boundary conditions are as follows: adiabatic walls (*3, 6, 7, 8, 5*), symmetry axis (*1*), interface wall (*4*) and porous pressure-outlet (*2*); the mesh is made by uniformly distributed quads with a 0.5 mm spacing.

As shown in Tab. 3, the reference geometry has a *H/D* ratio of 2 (*D = 2Ri*), while volumes are the optimal ones for atmospheric discharge pressure conditions (V. Krastev et al., 2023). All the performed CFD simulations are based on the following main assumptions:

a. the IMH-PCM tank domain is 2D axisymmetric;
b. the external tank boundaries (except for the hydrogen outlet boundary) are all adiabatic walls;
c. hydrogen is released from the IMH bed at a known and constant external pressure;
d. a porous section with a resistance coefficient k_{out} is added at the outlet, for mass flow damping and control;
e. gaseous hydrogen is assumed to follow the ideal gas law;
f. the IMH bed is considered as an isotropic porous medium with uniform porosity and permeability;
g. local thermal equilibrium is assumed to hold within the AB_5-H_2 system;
h. buoyancy is not considered for the heat transfer and melting phenomena within the PCMs;

https://doi.org/10.52202/077185-0067

i. properties of the PCMs are considered constant and equal to the average between solid and liquid.

Table 1. Main thermophysical and reaction properties of the AB_5-H_2 system.

Parameters	*Description*	*Values*
A_d	Plateau coefficient (desorption)	10.57
B_d	Plateau coefficient (desorption)	3704.6 K
C_d	Rate coefficient (desorption)	9.57 s^{-1}
$C_{p,g}$	Specific heat capacity (gas)	14890 J kg^{-1} K^{-1}
$C_{p,s}$	Specific heat capacity (solid)	419 J kg^{-1} K^{-1}
E_d	Activation energy (desorption)	16473 J mol^{-1}
ΔH_R	Enthalpy of reaction	30478 J mol^{-1}
k_b	Bed viscous resistance	10^8 m^{-2}
ε	Bed porosity	0.5
λ_g	Thermal conductivity (gas)	0.1815 W m^{-1} K^{-1}
λ_s	Thermal conductivity (solid)	2 W m^{-1} K^{-1}
μ_g	Dynamic viscosity (gas)	8.4 x 10^{-6} Pa s
ρ_{sat}	Saturated metal density	7259 kg m^{-3}
ρ_{emp}	H_2-free metal density	7164 kg m^{-3}
$w_{\%}$	Gravimetric capacity (bed only)	1.32 %
m_{AB5}	Metal mass	~ 0.422 kg
m_{H2}	H2 storage capacity	5.6 g

Table 2. Main thermophysical properties of the PCMs.

Parameters	*Description*	*PCM1*	*PCM2*
$C_{p,PCM}$	Specific heat capacity	2250 J kg^{-1} K^{-1}	2000 J kg^{-1} K^{-1}
L_f	Latent heat of fusion	296000 J kg^{-1}	224000 J kg^{-1}
T_m	Melting temperature	303 K	301 K
λ_{PCM}	Thermal conductivity	0.95 W m^{-1} K^{-1}	0.2 W m^{-1} K^{-1}
μ_{PCM}	Dynamic viscosity (liquid)	0.0042 Pa s	0.0031 Pa s
ρ_{PCM}	Density	1960 kg m^{-3}	825 kg m^{-3}
α	Thermal diffusivity	$2.15 \cdot 10^{-7}$ m^2 s^{-1}	$1.21 \cdot 10^{-7}$ m^2 s^{-1}
Pr	Prandtl number (liquid)	10	31

Table 3. Dimensional details of the considered jacket-type IMH-PCM tank.

Parameters	*Description*	*Values*
R_{H2}	H_2 outlet radius	0.5 cm
R_i	Internal radius	2.1 cm
R_e	External radius	3.2 cm
H	Height	8.5 cm
H/D	Slenderness	2
V_{MH}	MH volume (total)	118 cm^3
V_{PCM}	PCM volume	154 cm^3

The IMH-PCM system model has been implemented in ANSYS® Fluent (Ansys Inc., 2024b, 2024a), with ad-hoc developed User Defined Functions (UDFs) for the hydrogen release kinetics. In all the performed simulations, hydrogen discharge at constant external pressure is modelled while initial temperature is set everywhere at 1 K above the PCM solidification temperature. The numerical time step is set to 0.1 s, with a physical simulated time of 10^4 s. The computational grid is made of quad-uniform elements with a 0.5 mm spacing. Boundary conditions are listed in Fig. 1, while for further information on the modelling framework, the reader is redirected to previous publications from the authors (Bartolucci & Krastev, 2022; V. Krastev et al., 2023; V. K. Krastev & Falcucci, 2021).

https://doi.org/10.52202/077185-0067

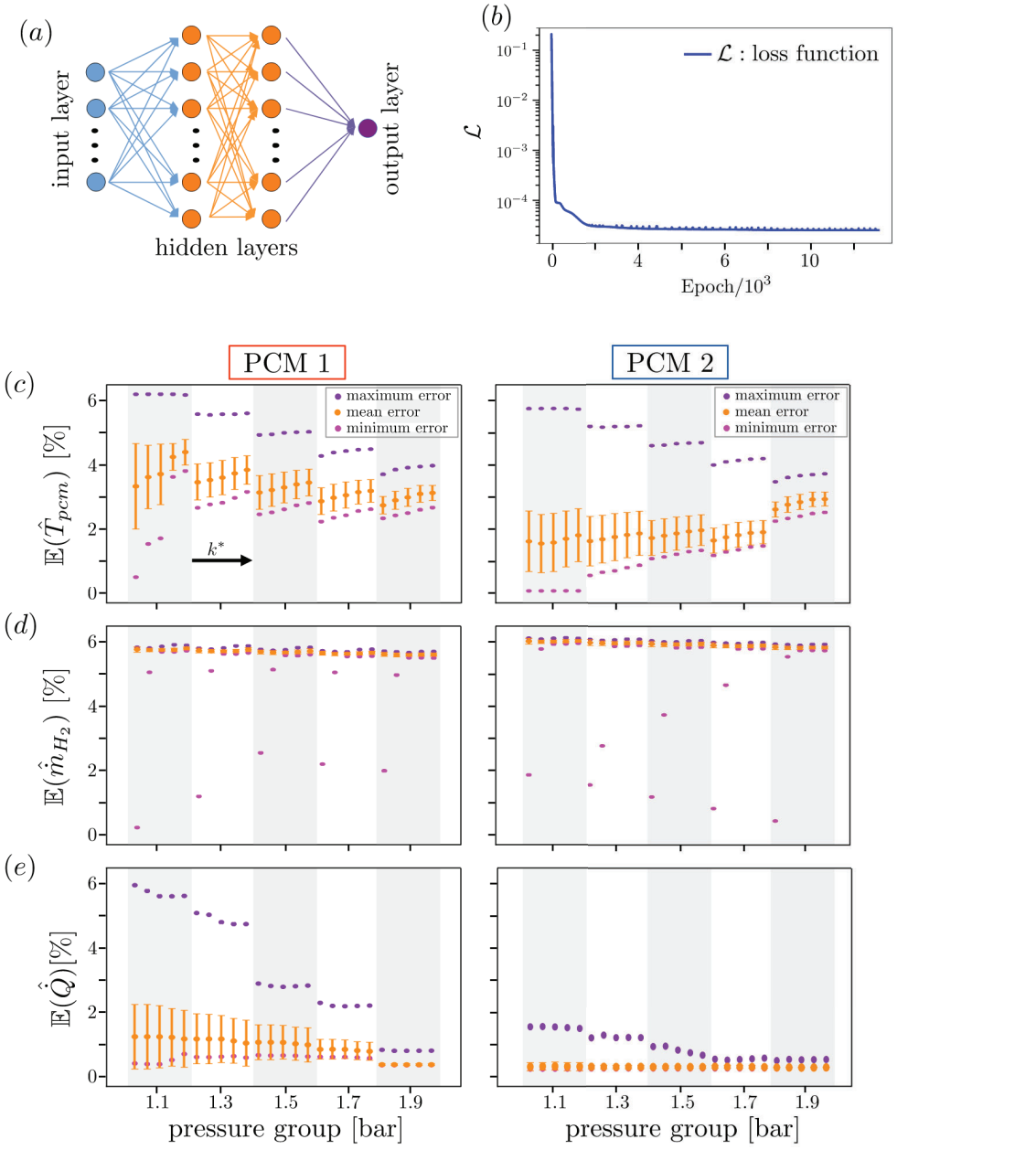

Figure 2: Neural Network architecture and training results. (a) Sketch of the NN architecture. The blue circles represent the feature that describe the PCMs and the operating condition, orange and violet circles represent the hidden layers and the output layer neurons, respectively, and the arrows represent the weights of the NN. **(b)** Loss function trend during the training phase.**(c,d,e)** Prediction error Eq. (4), for the normalised temperature $\hat{T}_{pcm}$, hydrogen mass flow rate $\hat{m}_{H_2}$ and the heat flux $\hat{Q}$ for each simulations used for the training for the two PCMs. The x-axis shows the different training pressure group. Each pressure has a corresponding set of five simulations, where each simulation uses a distinct value of the resistance ratio k^* (1, 10^2, 10^3, 10^4, 10^5). The effectiveness of the training phase is evaluated by analysing the maximum (violet dots), minimum (magenta dots), and the mean error of prediction obtained for each simulation. The orange line represents the standard deviation of the error.

2.2 Neural-Network definition

To demonstrate the capability of NNs to support the design of IMH-PCM systems, we develop a simple NN with the support of PyTorch libraries (Paszke et al., 2019), capable of predicting the evolution over time of the quantities of interest (*QoI*). The fully connected NN architecture includes an input layer,

https://doi.org/10.52202/077185-0067

two hidden layers with 100 neurons each and one output layer, see Fig. 1(a). The selection of the number of neurons and hidden layers is crucial for achieving optimal performance of the NNs. Since no exact theory exists on how to select the hyperparameters, we experimented with several network architectures, evaluating and comparing their performance both in the training and testing phase, adopting the NN configuration that provide the best balance between fitting the training and testing data. The ReLU activation function is adopted since satisfy several requirements: compared to other activation functions (*e.g.* sigmoid and hyperbolic tangent), ReLU has a simpler mathematical definition, leading to a faster training phase; the ReLU function helps to solve the vanishing gradient problem (Roodschild et al., 2020); finally, in the study here proposed the ReLU function provides better performance both in training and testing phase.

The input layer is designed to accommodate the features of the IMH-PCM system. A total of 10 features are chosen: external discharge pressure p and the porous resistance ratio $k^* = k_{out}/k_b$ defines the system operating conditions; 7 features, based on the properties shown in Tab. 2, that characterise the PCM material; the last one is the physical time t. In this preliminary study, features related to the IMH and geometry are not used and thus considered invariant in the system. It should be noted, however, that the approach is general and can be easily extended to incorporate variations of the IMH and system geometry.

For the NN training and test phases, a total of 100 transient CFD predictions are generated, considering 2 PCMs (PCM1 and PCM2), 10 external pressure levels (1.1 – 2.0 bar range) and five k^* values (from 1 to 10^5). For the training phase only, a subset of 50 CFD simulations is selected, considering only few combinations of p and k^* for both PCMs (p = 1.1, 1.3, 1.5, 1.7, 1.9 bar and k^* = 1, 10^2, 10^3, 10^4, 10^5), see Fig.2. The remaining 50 simulations were used for the testing phase.

For better results readability, all features are scaled to obtain values between 0 and 1, according to the following equation written for the generic feature x_i

$$\widehat{x_i} = \frac{x_i - x_{i,min}}{x_{i,max} - x_{i,min}}, \tag{1}$$

where $\widehat{x_i}$ is the normalised feature, $x_{i,min}$ and $x_{i,max}$ are the minimum and maximum values of x_i, respectively. For k^* only, a log_{10} normalization has been applied instead:

$$\widehat{k_i^*} = \frac{log_{10}\, k_i^* - log_{10}\, k_{i,min}^*}{log_{10}\, k_{i,max}^* - log_{10}\, k_{i,min}^*}. \tag{2}$$

The data normalization is also an important aspect during the training phase for NNs. Data normalization allows to compare, as in our study, features with different scales ensuring that each feature has, for instance, a comparable impact on the weight update during the backpropagation.

The training is then performed minimizing the sum-of-square error function $\mathcal{L}(x,y)$ (loss function) given by

$$\mathcal{L}(x,y) = \frac{1}{2}\sum_{i=1}^{N} \left|\left| y(\widehat{x_i}) - \hat{\mathrm{f}}(\mathrm{x_i}) \right|\right|^2, \tag{3}$$

where, N is the total number of samples in the data set, $y(x_i)$ is the predicted value, and $\hat{f}(x_i)$ is the normalised corresponding actual target value.

To optimise the NN's parameters, the backpropagation algorithm is employed. This process involves computing the gradient of $\mathcal{L}(x,y)$ with respect to the model parameters and adjusting the parameters using the ADAM optimization algorithm. The model selection was made using the k-fold cross-validation method. The training dataset is divided into k groups (folds), one of those groups is used as validation set and the remaining k-1 folds are used for the training for $1.5x10^4$ epochs. Moreover, to reduce the risk of overfitting, a 10% dropout is applied (Srivastava et al., 2014). In Fig. 2(b), the loss function trend for the selected model is reported. To give a clear quantification of the difference between

https://doi.org/10.52202/077185-0067

the prediction $y(\hat{x}_i)$ and the real target value $f(\hat{x}_i)$ (*i.e.* the NN error), the error $\mathbb{E}(\mathrm{y},\mathrm{f})$ is defined as follows:

$$\mathbb{E}(y) = 100\left|y(\hat{x}_i) - \hat{f}(x_i)\right|. \quad (4)$$

It is worth noting that, since the maximum value of a quantity normalised according to Eq.(1) is 1, the error $\mathbb{E}(\mathrm{y},\mathrm{f})$ multiplied by 100 is a percentage. In Fig. 2.(c-e) the minimum, maximum and mean errors $\mathbb{E}$ for the two PCMs and for the three normalised QoIs (PCM temperature $\hat{T}_{pcm}$, hydrogen mass flow rate $\hat{m}_{H_2}$ and the heat flux $\hat{\hat{Q}}$) is reported. For each pressure and resistances k^* , the mean error is systematically lower than 6% confirming the training success. A detailed discussion about the training phase results is presented in the Results section.

3 RESULTS

As mentioned above in Section 2.2, the NN training was carried out considering both the PCMs and only some values of pressure *p* and relative resistance k^* (see Fig. 2 and the Materials & Methods section for details).
For the *PCM1* temperature, Fig.2(c), the error during the training phase decreases as the external pressure increases, while it remains approximately constant as the value of k^* increases. For both the PCMs, as the pressure increases, the prediction appears more accurate and reliable since the standard deviation decreases and the mean error is always lower than 4%. A similar behaviour is observed also in the trends of the heat flux errors for *PCM1*, see the left side of Fig. 2(e), while for the *PCM2* the errors are consistently less than 1%, right side of Fig. 2(e). For the hydrogen mass flow rate, Fig. 2(d), the minimum and maximum errors converge to a single point around 6% for both the PCMs.

The test phase is then conducted using pressures *p* never used during the training phase, see Fig.3. In this Figure, a general trend can be observed: increasing the external pressure, the mean error and the error standard deviation decrease (*i.e.* better predictions) and also better performances are obtained for *PCM2*. The quality prediction of QoIs for the second PCM are related to the dynamics of the system in which this PCMs are used. As can be observed in Fig. 4, the dynamics of the *IMH-PCM2* system is slower with respect to the dynamics of *IMH-PCM1*, especially at the beginning of the hydrogen discharge phase, see also inset Fig. 4(c). For the same reasons, when k^* and *p* increase, the prediction errors decrease. This means that, as expected, systems with smooth and slow dynamics are easier to predict accurately for our NN model.

As previously stated, in Fig. 4 a direct comparison between NN and CFD results for few cases is shown. Specifically, to highlight the effectiveness of the model, cases are presented where low external pressure values (fast dynamics) were used in conjunction with high values of the parameter k^* (slow dynamics). In Fig.4(a,d), the normalised temperature $\hat{T}_{PCM}$ of both the PCMs is reported and the trends are well reproduced by the neural network. The NN has also demonstrated the ability to predict, with good approximation, the PCM temperature behaviour even when low pressure values are applied (blue solid lines in Fig.4(a,d)). Furthermore, the NN is also able to effectively capture and replicate the hydrogen mass flow rate and the exchanged heat flux across the entire time range, Fig.4(b-f). Moreover, despite the neural network is trained to reproduce the long-term performance of the system over a time span of 10^4 s, it is even capable of accurately describing behaviours occurring within the initial hundreds of seconds (~1% of the total time) characterised by a faster dynamics, see Fig.4(b,e) and insets in Fig4(c,f). In turn, this implies the ability of neural networks to understand and reproduce the hidden mechanisms behind the physical connections that exist between the analysed variables.
It is worth also noting that, the NN remarkable properties of predicting the faster dynamics in IMH-PCM systems (if compared with the utilization time of this kind of system) and the long-term trend of QoIs, may be attributed to the specific focus on study only the hydrogen release scenario. However,

https://doi.org/10.52202/077185-0067

when complex load profiles are integrated and both hydrogen accumulation and release are considered, targeted training can be exploited to further enhance the neural network performance.

Finally, the NN model is tested on a third PCM (*PCM3*), with main thermophysical properties listed in Table 4. For the reader convenience and to highlight the difference between the PCMs, a radar diagram is reported in Fig. 5(a). The diagram shows five derived quantities that fully describe the PCMs and focusing on the absolute values, *PCM3* exhibits intermediate properties between *PCM1* and *PCM2*. Consequently, it proves to be an excellent test for verifying the model's capabilities as a regressor. In Fig. 5(b) the errors for the prediction of the three QoIs for *PCM3* are reported. The third PCM is tested for one pressure level, $p = 1.5$ bar, and for two $k^* = 10^4$-10^5. In line with the observations for *PCM1* and *PCM2*, the prediction errors for *PCM3* remain lower for hydrogen the mass flow rate and the exchanged heat flux compared to those observed for the temperature. Despite this, the overall prediction error remains below 10%, which is further confirmation of the model's strong performance as a regressor.

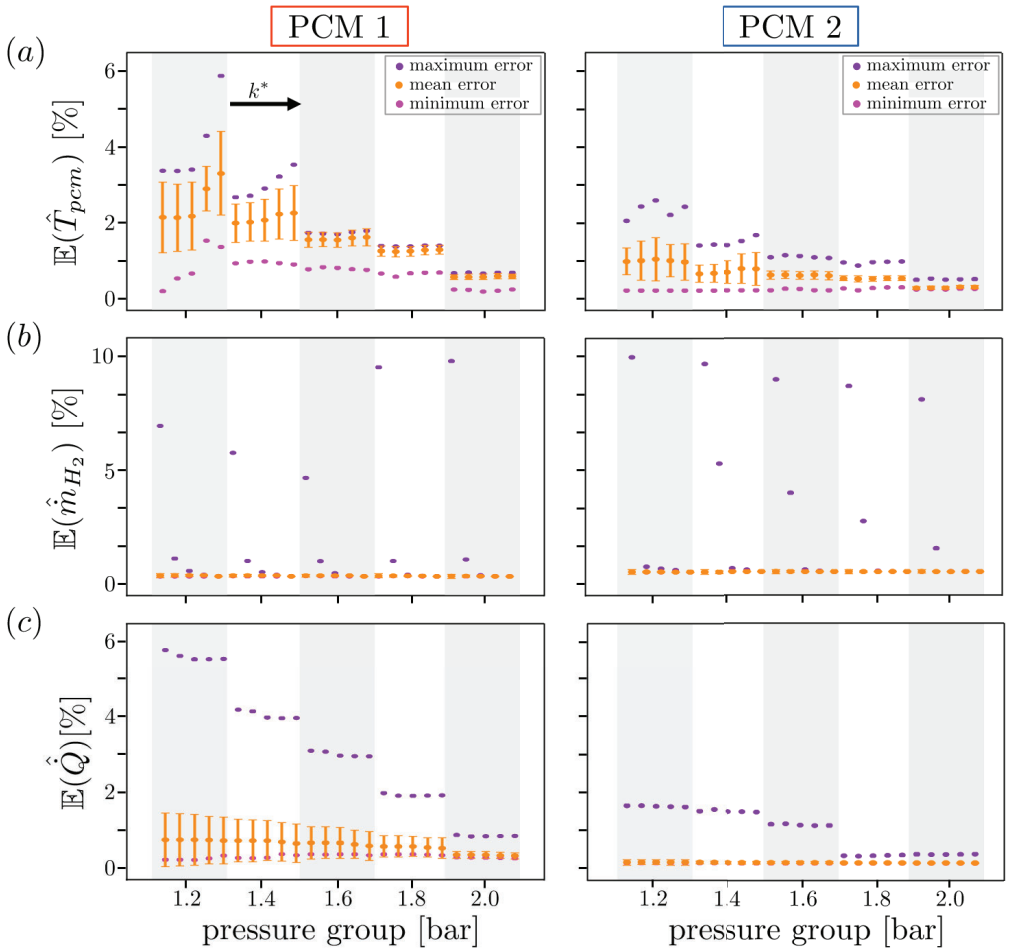

Figure 3: Neural network prediction errors. The panels represent the error in the test prediction for the two PCMs for the normalised temperature $\hat{T}_{pcm}$ (panel (a)), hydrogen mass flow rate $\hat{\dot{m}}$ (panel (b)), and heat flux $\hat{\dot{Q}}$ (panel (c)). The x-axis represents the pressure groups and for each group the error for five simulations, that differ for the resistance ratio k^*, is reported. The minimum, maximum and mean errors are represented using the magenta, violet and orange dots, respectively. The orange segment represents the error standard deviation (in panel (b) the standard deviation is smaller than the symbol used for the mean error).

https://doi.org/10.52202/077185-0067

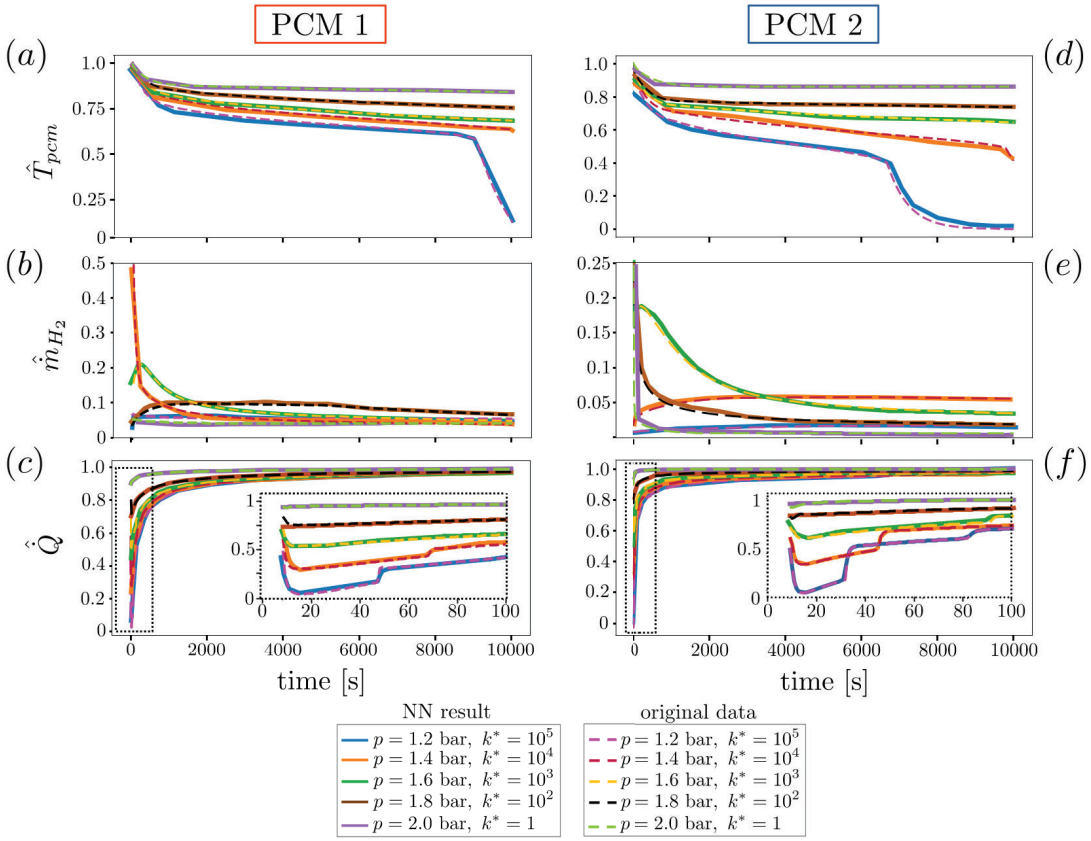

Figure 4: Neural network prediction example during the test phase. (a-c) Comparison between the NN prediction and the original CFD data for the normalised temperature (panel (a)), hydrogen mass flow rate (panel (b)) and thermal power (panel (c)) for *PCM1*. The insets in panel (b) and (c) highlight the capability of the NN to predict faster dynamics in the initial hundreds of seconds. **(d-f)** Comparison between the predicted QoIs through the NN and the CFD simulation data. The insets in panel (e) and (f) shown the prediction of the NN within the first 100 s, where the dynamics of the system change rapidly.

Table 4. Main thermophysical properties of PCM3

Parameters	*Description*	*PCM3*
$C_{p,PCM}$	Specific heat capacity	2000 K kg^{-1} K^{-1}
L_f	Latent heat of fusion	132000 J kg^{-1}
T_m	Melting Temperature	302 K
λ_{PCM}	Thermal conductivity	0.5 W m^{-1}K^{-1}
μ_{PCM}	Dynamic viscosity (liquid)	0.05 Pa s
ρ_{PCM}	Density	1525 kg m^{-3}
α	Thermal diffusivity	1.6·10^{-7} m^{2}s^{-1}
Pr	Prandtl number (liquid)	200

https://doi.org/10.52202/077185-0067

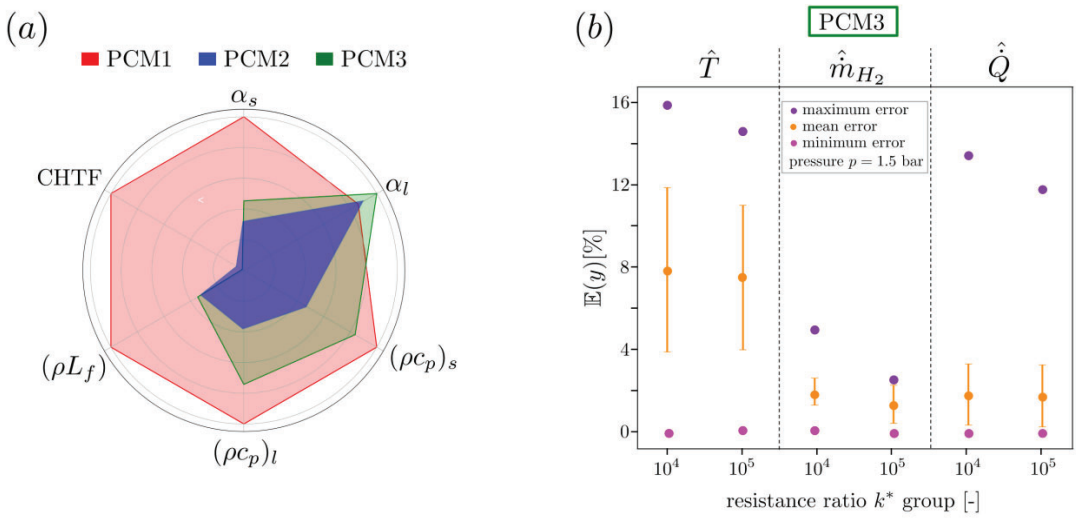

Figure 5: NN prediction for PCM3. (a) The radar diagram summarise the difference between the three PCMs in terms of: volumetric latent heat (ρL_f), volumetric heat capacity of the liquid phase $(\rho C_p)_l$, solid phase volumetric heat capacity $(\rho C_p)_s$, liquid thermal diffusivity α_l, solid thermal diffusivity α_s, and convective heat transfer factor (CHTF). For a detailed discussion on those parameters, the reader is referred to *(Bartolucci & Krastev, 2022)*. The *PCM1, PCM2* and *PCM3* are represented by red, blue and green areas, respectively. **(b)** Prediction errors for the normalised temperature, hydrogen mass flow rate and heat flux, for the *PCM3*. The x-axis represent simulation groups defined through the resistance ratio k^*. All the simulations and prediction are performed at $p = 1.5$ bar.

4 CONCLUSIONS

In spite of the preliminary nature of the results shown above, the following concluding remarks can be drawn:

- the proposed NN approach is capable of accurately reproduce time-varying outputs from an IMH-PCM storage system, including hydrogen mass flow and the heat transfer between the hydride and PCM compartments;
- except for limited initial sharp transients, encountered in uncontrolled mass flow discharge cases (low k^*), the error in NN predictions is well within 10% compared to the initial high-fidelity CFD data used for training and testing;
- the data-driven model is able to predict the behaviour of the IMH-PCM system even for PCMs not used in the training phase keeping the error below the 10%.

The pathway towards a full-featured NN-based solver for IMH-PCM modelling will include: I) the extension of the training base with up to ~10^3 additional CFD-generated data sets; II) the refinement of the physics included (e. g. mass flow controller modelling) and III) testing within complex time-varying load profile scenarios.

NOMENCLATURE

NN	Neural Network	
IMH/MH	Intermetallic Metal Hydrides/Metal Hydrides	
PCM	Phase Change Material	
CFD	Computational Fluid Dynamics	
QoI	Quantity of Interest	
H	Height	[m]

https://doi.org/10.52202/077185-0067

D	Diameter	[m]
R_i	Internal Radius	[m]
R_e	External Radius	[m]
k	Viscous resistance	[m^{-2}]
A	Plateau coefficient (desorption)	[-]
B	Plateau coefficient (desorption)	[K]
C	Rate coefficient	[s^{-1}]
C_p	Specific heat capacity	[J kg^{-1} K^{-1}]
E	Activation energy	[J mol^{-1}]
ΔH_R	Enthalpy of reaction	[J mol^{-1}]
λ	Thermal conductivity	[W m^{-1} K^{-1}]
μ	Viscosity	[Pa s]
ρ	Density	[kg m^{-3}]
ε	MH porosity	[-]
$w_{\%}$	Gravimetric capacity	[%]
m	Mass	[kg]
k^*	Resistance ratio k_{out}/k_b	[-]
L	Latent heat of fusion	[J kg^{-1}]
T	Temperature	[K]
α	Thermal diffusivity	[m^2 s^{-1}]
Pr	Prandtl number	[-]
p	Pressure	[bar]
$\mathscr{L}$	Loss function	[-]
$\mathbb{E}$	Prediction eror	[-]
y	NN prediction	[-]
f	Target value	[-]
x	Generic feature	[-]
$\dot{m}$	Mass flow rate	[kg s^{-1}]
$\dot{Q}$	Heat flux	[W]
N	samples	[-]

Subscript

d	desorption
out	outlet
gas	gas
s	solid
b	bed
sat	saturated MH
emp	empty MH
AB5	$LaAB_5$-based alloy
H2	hydrogen
f	fusion
m	melting
i	feature
0	baseline
min	minimum
max	maximum

Superscript

^	normalised quantity

https://doi.org/10.52202/077185-0067

REFERENCES

Alqahtani, T., Mellouli, S., Bamasag, A., Askri, F., & Phelan, P. E. (2020). Thermal performance analysis of a metal hydride reactor encircled by a phase change material sandwich bed. *International Journal of Hydrogen Energy*, *45*(43), 23076–23092. https://doi.org/10.1016/j.ijhydene.2020.06.126

Ansys Inc. (2024a). *ANSYS® Academic Research CFD, Release 2024 R1, Fluent Theory Guide*. http://www.ansys.com

Ansys Inc. (2024b). *ANSYS® Academic Research CFD, Release 2024 R1, Fluent User's Guide*. http://www.ansys.com

Bartolucci, L., & Krastev, V. K. (2022). On the Thermal Integration of Metal Hydrides with Phase Change Materials: Numerical Simulation Developments towards Advanced Designs. *SAE Technical Papers*. https://doi.org/10.4271/2022-24-0018

Bouzgarrou, F., Mellouli, S., Alqahtani, T., & Algarni, S. (2022). Parametric study of a metal hydride reactor with phase change materials and heat pipes. *International Journal of Energy Research*, *46*(4), 4588–4598. https://doi.org/10.1002/er.7451

Chibani, A., Merouani, S., Gherraf, N., Ferhoune, I., & Benguerba, Y. (2022). Numerical investigation of heat and mass transfer during hydrogen desorption in a large-scale metal hydride reactor coupled to a phase change material with nano-oxide additives. *International Journal of Hydrogen Energy*, *47*(32), 14611–14627. https://doi.org/10.1016/j.ijhydene.2022.02.171

Drawer, C., Lange, J., & Kaltschmitt, M. (2024). Metal hydrides for hydrogen storage – Identification and evaluation of stationary and transportation applications. *Journal of Energy Storage*, *77*. https://doi.org/10.1016/j.est.2023.109988

El Mghari, H., Huot, J., Tong, L., & Xiao, J. (2020). Selection of phase change materials, metal foams and geometries for improving metal hydride performance. *International Journal of Hydrogen Energy*, *45*(29), 14922–14939. https://doi.org/10.1016/j.ijhydene.2020.03.226

Facci, A. L., Lauricella, M., Succi, S., Villani, V., & Falcucci, G. (2021). Optimized modeling and design of a PCM-enhanced h2 storage. *Energies*, *14*(6). https://doi.org/10.3390/en14061554

He, J. W., Shu, Z. Y., Huang, R. N., Liu, Z. Q., Huang, C., Cai, Y., & Zhao, F. Y. (2024). Numerical analysis and ANN performance prediction of solar composite ventilation wall for built environment regulation. *Energy Conversion and Management*, *311*. https://doi.org/10.1016/j.enconman.2024.118512

Jany, P., & Bejan, A. (1988). Scaling theory of melting with natural convection in an enclosure. *Int. J. Heat Mass Transfer*, *31*(6), 1221–1235.

Krastev, V., Bella, G., Falcucci, G., Bartolucci, L., Cordiner, S., & Mulone, V. (2023). Power Vs. Capacity Performances of Thermally Integrated MH-PCM Hydrogen Storage Solutions: Current Status and Development Perspectives. *36th International Conference on Efficiency, Cost, Optimization, Simulation and Environmental Impact of Energy Systems, ECOS 2023*, 2183–2193. https://doi.org/10.52202/069564-0197

Krastev, V. K., & Falcucci, G. (2021). Comparison of enthalpy-porosity and lattice Boltzmann-phase field techniques for the simulation of the heat transfer and melting processes in LHTES devices. *E3S Web of Conferences*, *312*, 01002. https://doi.org/10.1051/e3sconf/202131201002

Kukkapalli, V. K., Kim, S., & Thomas, S. A. (2023). Thermal Management Techniques in Metal Hydrides for Hydrogen Storage Applications: A Review. *Energies*, *16*(8). https://doi.org/10.3390/en16083444

Maalla, A., Dahari, M., Chaturvedi, R., Fouad, Y., Abdullaev, S., Farag, A., Alkhayyat, A., & Abdo, G. M. (2024). Artificial neural network-based optimization of heat absorption process of phase change materials in a novel-designed finned-plate latent heat storage system. *Journal of Energy Storage*, *86*. https://doi.org/10.1016/j.est.2024.111256

Nguyen, H. Q., Mourshed, M., Paul, B., & Shabani, B. (2022). An experimental study of employing organic phase change material for thermal management of metal hydride hydrogen storage. *Journal of Energy Storage*, *55*. https://doi.org/10.1016/j.est.2022.105457

https://doi.org/10.52202/077185-0067

Nguyen, H. Q., & Shabani, B. (2021). Review of metal hydride hydrogen storage thermal management for use in the fuel cell systems. *International Journal of Hydrogen Energy*, *46*(62), 31699–31726. https://doi.org/10.1016/j.ijhydene.2021.07.057

Ouro-Koura, H., Jung, H., Li, J., Borca-Tasciuc, D.-A., Copping, A. E., & Deng, Z. D. (2024). Predictive model using artificial neural network to design phase change material-based ocean thermal energy harvesting systems for powering uncrewed underwater vehicles. *Energy*, *301*, 131660. https://doi.org/10.1016/j.energy.2024.131660

Pasquini, L., Sakaki, K., Akiba, E., Allendorf, M. D., Alvares, E., Ares, J. R., Babai, D., Baricco, M., Bellosta Von Colbe, J., Bereznitsky, M., Buckley, C. E., Cho, Y. W., Cuevas, F., De Rango, P., Dematteis, E. M., Denys, R. V., Dornheim, M., Fernández, J. F., Hariyadi, A., … Yartys, V. A. (2022). Magnesium- and intermetallic alloys-based hydrides for energy storage: Modelling, synthesis and properties. *Progress in Energy*, *4*(3). https://doi.org/10.1088/2516-1083/ac7190

Paszke, A., Gross, S., Massa, F., Lerer, A., Bradbury Google, J., Chanan, G., Killeen, T., Lin, Z., Gimelshein, N., Antiga, L., Desmaison, A., Xamla, A. K., Yang, E., Devito, Z., Raison Nabla, M., Tejani, A., Chilamkurthy, S., Ai, Q., Steiner, B., … Chintala, S. (2019). *PyTorch: An Imperative Style, High-Performance Deep Learning Library*.

Roodschild, M., Gotay Sardiñas, J., & Will, A. (2020). A new approach for the vanishing gradient problem on sigmoid activation. *Progress in Artificial Intelligence*, *9*(4), 351–360. https://doi.org/10.1007/s13748-020-00218-y

Şenol, G., Selimefendigil, F., & Öztop, H. F. (2024). A review on nanofluid, phase change material and machine learning applications for thermal management of hydrogen storage in metal hydrides. *International Journal of Hydrogen Energy*, *68*, 1178–1208. https://doi.org/10.1016/j.ijhydene.2024.04.215

Sreeraj, R., Aadhithiyan, A. K., & Anbarasu, S. (2022). Integration of thermal augmentation methods in hydride beds for metal hydride based hydrogen storage systems: Review and recommendation. *Journal of Energy Storage*, *52*. https://doi.org/10.1016/j.est.2022.105039

Srivastava, N., Hinton, G., Krizhevsky, A., & Salakhutdinov, R. (2014). Dropout: A Simple Way to Prevent Neural Networks from Overfitting. *Journal of Machine Learning Research*, *15*, 1929–1958.

ACKNOWLEDGEMENTS

The authors acknowledge partial support from the National Center for HPC, Big Data and Quantum Computing, Project CN_00000013 - CUP: E83C22003230001, Mission 4 Component 2 Investment 1.4, funded by the European Union - NextGenerationEU.

V. K. K. and G. F. wish to acknowledge support from Project PRIN 2022F422R2 - CUP: E53D23003210006, funded by the European Union - NextGenerationEU.

G. F. wishes to acknowledge support from Project PRIN PNRR P202298P25 - CUP: E53D23016990001, funded by the European Union - NextGenerationEU.

M. B. wishes to acknowledge support from Project ECS 0000024 Rome Technopole - CUP: B83C22002820006, NRP Mission 4 Component 2 Investment 1.5, Funded by the European Union – NextGenerationEU

https://doi.org/10.52202/077185-0067